energy&fuels

Article

pubs.acs.org/EF

Regenerable Sorbent with a High Capacity for Elemental Mercury Removal and Recycling from the Simulated Flue Gas at a Low Temperature

Zan Qu, Jiangkun Xie, Haomiao Xu, Wanmiao Chen, and Naiqiang Yan*

School of Environmental Science and Engineering, Shanghai Jiao Tong University, 800 Dongchuan Road, Shanghai 200240, People's Republic of China

Supporting Information

ABSTRACT: To remove and recycle elemental mercury from flue gas, a serial of Ce−Mn binary metal oxides was prepared and tested as the regenerable sorbents for mercury capture. $Ce_{0.5}Mn_{0.5}O_y$ showed the best performance at 100 °C (about 5.6 mg g^{-1} adsorption capacity), and Ce−Mn binary metal oxides could adsorb more elemental mercury than MnO_y. Furthermore, it was found that captured mercury can be released from the sorbent in the form of elemental mercury by heating to 350 °C. Meanwhile, the sorbent can be regenerated and repeatedly used. Powder X-ray diffractometer (PXRD), transmission electron microscopy (TEM), hydrogen temperature-programmed reduction (H_2-TPR), ammonia temperature-programmed desorption (NH_3-TPD), X-ray photoelectron spectroscopy (XPS), and nitrogen adsorption methods were employed to characterize the sorbents. A model based on mercury temperature-programmed desorption (Hg-TPD) data was built to calculate mercury desorption activation energy from the sorbent. Additionally, the impacts of the temperature and flue gas components on the adsorption capacity were investigated. NO had negligible impact on mercury adsorption, while the presence of SO_2 slightly inhibited the capability of sorbents for mercury capture. The results indicated that Ce−Mn binary metal oxides are a promising sorbent for the mercury removal and recycling from flue gas.

1. INTRODUCTION

Mercury is one of the most hazardous pollutants as a result of its neurological toxicity, bioaccumulation, and persistence.[1] With the agreement of the Minamata Convention on Mercury in 2013, the emission of mercury from coal-fired power plants has become a serious concern in China.[2,3] Recently, the revised emission standard of air pollutants for thermal power plants of China has come into force, in which the limited value of mercury emission has been capped. Mercury emission control will be the trend for the coal-fired power plants.

To date, the main technologies for mercury emission control fall into two groups: powder activated carbon (PAC) injection and co-benefit of selective catalytic reduction (SCR) and wet flue gas desulfurization (W-FGD) system (Hg^0 was catalytically oxidized into Hg^{2+} on the SCR catalyst and then scavenged by W-FGD).[4−8] However, the co-benefit of SCR and W-FGD will drive mercury from the gas phase to the liquid or solid phase, which may cause the secondary pollution.[9,10] PAC displays high efficiency for mercury removal, but the regenerating activated carbon (AC) sorbents for further Hg capture is not an effective process, which limits its wide application.[11] Meanwhile, the commercial value of the fly ash is sacrificed by the PAC injection method.[12] Therefore, the development of a novel non-carbon sorbent with high mercury adsorption capacity and facile regeneration ability has attracted more and more attention.[13−15] Especially, developing high-performance sorbents for mercury capture downstream of the electrostatic precipitator (ESP) or fabric filter (FF) at a low temperature (<200 °C) is of great significance.[16]

High adsorption capability and proper oxidation ability were two indispensible properties for excellent mercury sorbent. Manganese oxides were reported to have excellent redox activity and were widely investigated for environmental remediation and fuel cell.[17,18] Meanwhile, ceria has been studied extensively because of its oxygen storage and redox properties.[19−22] Among these materials, the combination of manganese oxide and cerium oxide has been proven to be an excellent catalyst for Hg^0 catalytic oxidation.[23−25] Few research on Ce−Mn binary metal oxides for mercury adsorption has yet been reported. Thus, how Ce−Mn binary metal oxides will perform as a mercury sorbent attracts our interest.

In this research, a serial of Ce−Mn binary metal oxides was synthesized as novel mercury sorbents. The impact of flue gas components on their adsorption capacity and the regenerability of the sorbent were investigated. According to the experiment and characterization results, the possible mechanism of mercury adsorption and desorption was discussed. A model for calculation of mercury desorption activation energy from the sorbent was also built.

2. MATERIALS AND METHODS

2.1. Preparation of Sorbents. A template method was employed to synthesize Ce−Mn binary metal oxides. F127 is a kind of triblock copolymer (EO_{106}−PO_{70}−EO_{106}, Sigma-Aldrich, P2443-250G), which is often used in mesoporous material synthesis. Herein, it was used as a template in this research. In a typical synthesis procedure, 0.9 g of F127 was dissolved in 10 mL of ethanol under stirring and heated to 40 °C. Then, 2.5 mmol of $Ce(NO_3)_3{\cdot}6H_2O$ and 2.5 mmol of

Received: April 21, 2015
Revised: August 23, 2015
Published: August 24, 2015

DOI: 10.1021/acs.energyfuels.5b00868
Energy Fuels 2015, 29, 6187−6196

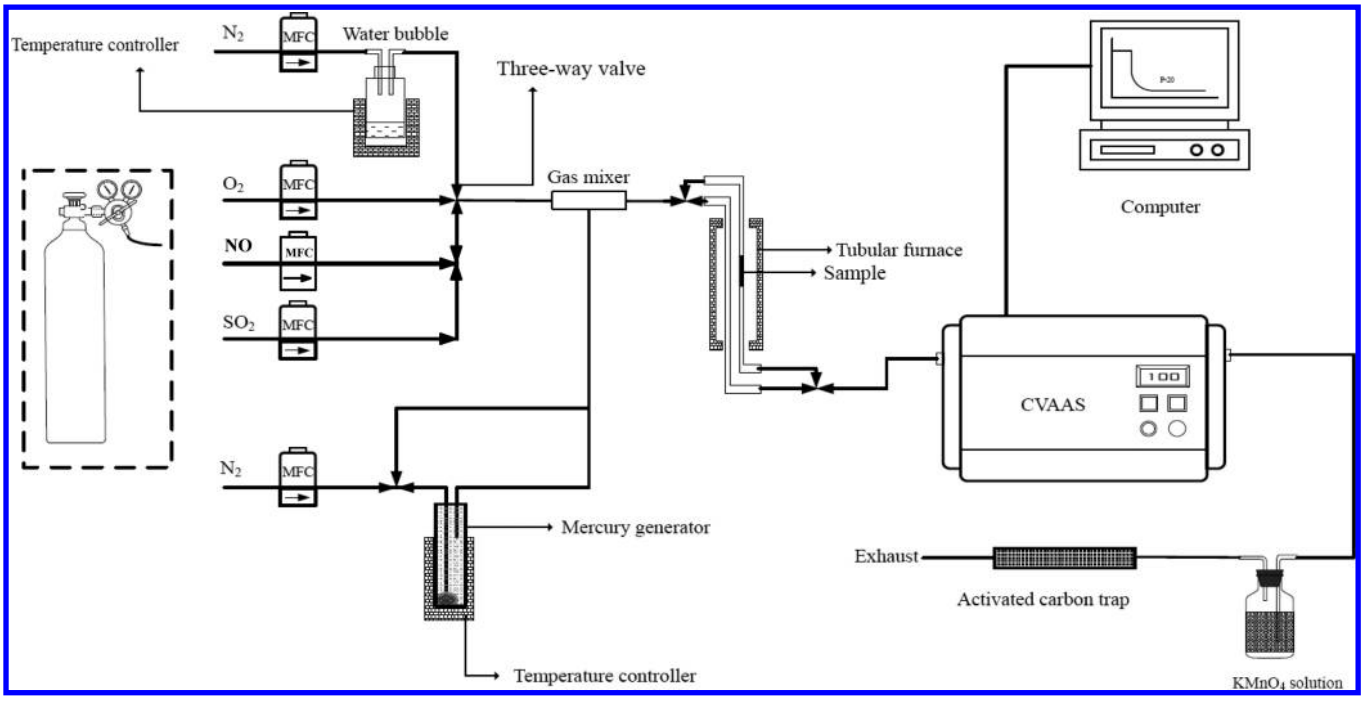

Figure 1. Sketch of the flow process for sorbent mercury capacity evaluation.

$Mn(NO_3)_2$ were added to the solution. After that, the solution was stirred for 2 h and aged at 40 °C for 2 days and 100 °C for 1 day. Finally, the sample was calcined at 500 °C for 5 h and was grounded to 40−60 mesh for the activity test. It was denoted as $Ce_{0.5}Mn_{0.5}O_y$, where y was the number of the corresponding oxygen atom, while 0.5 was the molar ratio of Ce/(Ce + Mn). With the control of different stoichiometric ratios, CeO_2, $Ce_{0.75}Mn_{0.25}O_y$, $Ce_{0.25}Mn_{0.75}O_y$, and MnO_y were prepared in the same procedure.

2.2. Characterization of Adsorbents. Powder X-ray diffraction patterns (PXRDs) were measured on a Rigaku D/max-2200/PC powder diffractometer using Cu Kα radiation (40 kV and 20 mA). The scanning range was from 10° to 80° with a scanning velocity of 7° min^{-1}. The crystal phases in the samples were identified with the help of Joint Committee on Powder Diffraction Standards (JCPDS) data files with the file number 34-0394. The microstructure of catalysts was analyzed by transmission electron microscopy (TEM). Samples were dispersed in ethanol with strong sonication before analysis, and the data were collected on JEM-2100 (20 kV) with energy-dispersive X-ray spectroscopy (EDX) as an accessory. Nitrogen adsorption and desorption data were obtained on a nitrogen adsorption apparatus (Quantachrome Nova 2200e) at −196 °C (temperature of the liquid nitrogen bath). All samples were degassed for 3 h at 200 °C before the test. Specific surface areas were calculated through the Brunauer−Emmett−Teller (BET) method. Hydrogen temperature-programmed reduction (H_2-TPR) and ammonia temperature-programmed desorption (NH_3-TPD) were carried out on a Chemisorp TPx 2920 instrument. The sorbents were degassed at 300 °C for 3 h under an Ar atmosphere before the H_2-TPR test, and the reducing gas was 10% H_2/Ar. For the NH_3-TPD test, the sorbent was degassed at 300 °C for 3 h under a helium atmosphere and then was cooled. Physically adsorbed NH_3 was purged out by helium before the test. The X-ray photoelectron spectroscopy (XPS) was performed on an AXIS Ultra^{DLD} (Shimadzu−Kratos) spectrometer with Al Kα as the excitation source. The C 1s line at 284.6 eV was taken as a reference for the binding energy calibration. An ion chromatogram was taken on the EP-1000 ion chromatograph (Beijing Li Yuan Electronic Co., Ltd., China). The mercury temperature-programmed desorption (Hg-TPD) experiment was carried out in a temperature-programmed furnace (the same furnace used in the adsorption process), and desorbed mercury was detected by the cold vapor atomic absorption spectrometer (CVAAS) detector (SG921, Jiangfen, Ltd., China).

2.3. Hg^0 Adsorption Experiments. The mercury adsorption test over the sorbents was performed with a bench-scale adsorption test system mainly containing an elemental mercury permeation tube, a packed-bed reactor with two parallel blank tubes, a CVAAS, and an online data acquisition system. The temperature of the reactor was controlled by a tubular furnace. N_2 was used as the carrier gas to yield a stable concentration of elemental mercury. Before the test, the mercury permeation tube was bypassed to calibrate the signal baseline and then carrier gas was diverted into the mercury permeation tube to generate a stable mercury concentration. Afterward, gaseous influent with a stable concentration of elemental mercury was diverted into the packed-bed reactor and the breakthrough curves were recorded by an online data acquisition system. The reactor was packed with a certain amount of sorbents (20 mg), and quartz wool was used as the support to prevent the loss of sorbents. The packed bed apparatus is similar to the reactor employed previously for mercury capacities.[26] To build a mercury balance, a reducing bottle containing $SnCl_2$ solution was placed on the outlet of the first CVAAS detector, and another CVAAS detector was put in tandem with the first CVAAS detector. It was found that two detectors displayed almost the same signal. It meant that Hg^{2+} in the effluent was negligible. To testify this, a mercury analyzer (Lumex RA915+, Russia) was employed to measure adsorbed mercury on the sorbent. A good mercury mass balance was achieved (relative deviation with calculation result was less than 5%). Hence, the influent mercury should be equal to mercury adsorbed on the sorbent surface plus elemental mercury in the effluent. The process flow of adsorption experiments is sketched in Figure 1.

To investigate the effect of flue gas components, the area of breakthrough curves of elemental mercury on $Ce_{1-x}Mn_xO_y$ during the test time (10 h) was integrated and the adsorption capacities of mercury were calculated according to eq 1. Adsorption capacity was defined as the mass of elemental mercury that was conversed into HgO or other forms on unit mass of sorbent. It was calculated as follows in this experiment:

$$Q = \frac{1}{m}\int_{t_0}^{t_1} (Hg^0{}_{inlet} - Hg^0{}_{outlet}) f \, dt \quad (1)$$

where Q is the adsorption capacity, m is the mass of sorbents (20 mg in this experiment), f denotes the flow rate of the influent, and t_0 and t_1 represent the initial and ending test times of the breakthrough curves, respectively.

DOI: 10.1021/acs.energyfuels.5b00868
Energy Fuels 2015, 29, 6187−6196

The total flow rate of gaseous influent was controlled at 200 mL min^{-1} containing 1.05 (±0.07) mg m^{-3} of elemental mercury and 4% O_2 (v/v), and the flow rate was balanced with N_2. A high mercury concentration was used here for time saving. The adsorption capacity of the prepared sorbent was relatively high. It would take several days for only one breakthrough curve if the mercury concentration is low. Consequently, a high concentration mercury was used to investigate the relative adsorption capability of the sorbents for mercury capture within 10 h. The experiments were carried out at a temperature range from 100 to 300 °C to investigate the influence of the temperature on sorbent adsorption capacity. The gas space velocity was about 1.0 × 10^5 h^{-1}. To test the influence of NO and SO_2, 500 ppm of NO or SO_2 was introduced into the gaseous influent through a mass flow controller and the total flow rate was also balanced with N_2. The elemental mercury concentrations of gaseous influent and effluent were continuously measured by a CVAAS (SG921, Jiangfen, Ltd., China), which was calibrated by a Lumex RA 915+ mercury analyzer.

For spent sorbent regeneration, the typical flow process was as follows: spent sorbent was purge with nitrogen until the effluent mercury signal decreased to the baseline level (in the same furnace). Then, the temperature was elevated to 350 °C, and the signal of effluent mercury was collected (the purge gas was high-purity nitrogen, and the flow rate was controlled at 200 mL min^{-1} in this experiment).

For Hg-TPD, the process was the same as the regeneration process, except that the temperature was programmed.

3. RESULTS AND DISCUSSION

3.1. Characterization of Adsorbents. The structure and phase composition of synthesized CeO_2, MnO_y, and Ce−Mn binary metal oxides are shown in Figure 2. As-prepared CeO_2 could be indexed as a face-centered cubic structure [space group *Fm*3*m* (225)] which matched well with PDF card (PDF file number 34-0394), while synthesized MnO_y could be indexed as well-defined cubic Mn_2O_3 [space group $Ia\bar{3}$ (206), PDF file number 41-1442]. With the increase of the manganese ratio (x) in $Ce_{1-x}Mn_xO_y$, the peak density decreased along with the broadening of the half peak width. Accordingly, the crystal size became smaller after forming binary metal oxides compared to single metal oxides. In other words, pure manganese oxide particles tended to aggregate, and formation of binary metal oxides with cerium could inhibit the grain growth. When the addition ratio (x) was below 0.5 [Mn/(Ce + Mn), mol mol^{-1}], only a face-centered cubic phase could be observed and no peaks corresponding to Mn_2O_3 or other forms of manganese oxides could be found from PXRD patterns. Additionally, the (111) peaks were found shifting slightly toward a higher angle with the increase of the manganese ratio, and this result was consistent with the reference, which concluded that solid solution was formed.[27]

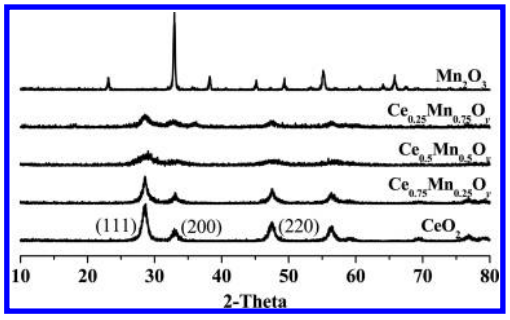

Figure 2. PXRD patterns of $Ce_{1-x}Mn_xO_y$ (x = 0, 0.25, 0.5, 0.75, and 1).

As shown in TEM images (Figure 3), synthesized CeO_2, $Ce_{0.5}Mn_{0.5}O_y$, and Mn_2O_3 were all nanosized particles with different sizes. The particle sizes of CeO_2 and $Ce_{0.5}Mn_{0.5}O_y$ were about 15 and 5 nm, respectively. While the size of synthesized Mn_2O_3 was much bigger (about 40 nm), this could be attributed to the tendency to aggregate for its particles. The variation trend of the crystal size was consistent with the result calculated through the Scherrer equation based on PXRD data. Additionally, according to the inset, only polycrystalline rings could be seen from the energy-dispersive spectrometry (EDS) images of synthesized CeO_2 and $Ce_{0.5}Mn_{0.5}O_y$. In contrast, both the single-crystal matrix and polycrystalline ring could be seen in the diffraction spectrum of MnO_y, which meant that the single crystal and polycrystal coexisted in synthesized Mn_2O_3. This could explain why MnO_y had the high degree of crystallinity, as shown in PXRD patterns. It could be concluded that pure manganese oxides tended to aggregate under the preparing condition. The formation of Ce−Mn binary metal oxides could prevent the aggregation of crystal particles. Consequently, a smaller particle size would be obtained. This smaller size could provide a higher contacting surface for adsorbate and might benefit the adsorption performance.

As shown in Table 1, the specific area of CeO_2 was approximately 81 m^2 g^{-1}, while Mn_2O_3 was only 10 m^2 g^{-1}. The specific surface areas changed with the doping of cerium, and $Ce_{0.5}Mn_{0.5}O_y$ had the largest specific surface area among the prepared Ce−Mn binary metal oxides. The coexisting cerium and manganese oxides facilitated the formation of smaller particles. The result was testified by the TEM image, in which $Ce_{0.5}Mn_{0.5}O_y$ showed the smallest particle size. This was also consistent with the result calculated by the Scherrer equation based on PXRD data. Obviously, varying the ratio of cerium in

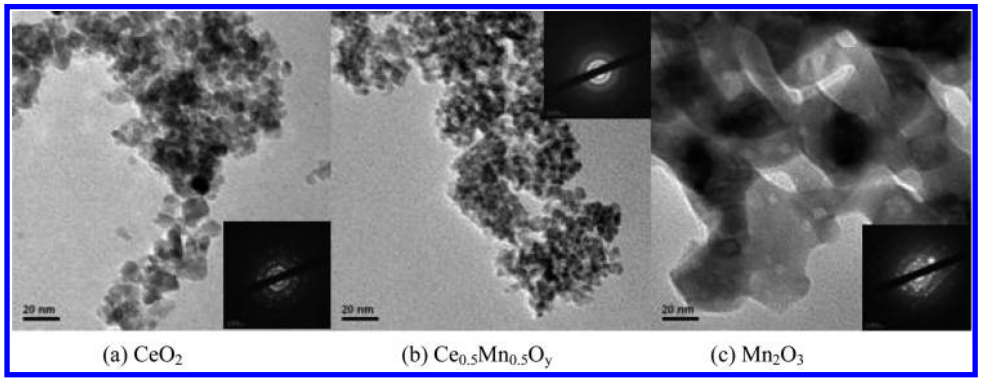

Figure 3. TEM images of $Ce_{1-x}Mn_xO_y$ (x = 0, 0.5, and 1).

DOI: 10.1021/acs.energyfuels.5b00868
Energy Fuels 2015, 29, 6187−6196

Table 1. N_2 Adsorption and Desorption Results of $Ce_{1-x}Mn_xO_y$

sample	BET specific surface area ($m^2\ g^{-1}$)
CeO_2	81
$Ce_{0.75}Mn_{0.25}O_y$	64
$Ce_{0.5}Mn_{0.5}O_y$	112
$Ce_{0.25}Mn_{0.75}O_y$	66
MnO_y	10

Ce−Mn binary metal oxides was an effective way to adjust its specific surface area.

In addition, the H_2-TPR technique was employed to investigate the reducibility of the prepared sorbents. As shown in Figure 4, single metal oxide CeO_2 had two reducing peaks centered at 550 and 800 °C. Comparatively, reducing peaks of prepared Mn_2O_3 emerged at about 380 and 490 °C, indicating that its reducibility is higher than that of CeO_2. For binary metal oxides, with the increase of the manganese content, the reducing peaks at a low temperature strengthened, while peaks at a high temperature shrank. Furthermore, the reducing peaks of $Ce_{0.75}Mn_{0.25}O_y$ and $Ce_{0.5}Mn_{0.5}O_y$ shifted toward a lower temperature. It indicated that Ce−Mn binary metal oxide was the solid solution and not the combination of two separate metal oxides. The strong interaction between cerium and manganese oxides could significantly enhance the reducibility of the sorbent. With a further increase of manganese, the shape and position of the reducing peaks seemed to be a simple summation of CeO_2 and Mn_2O_3. That may be because a high manganese content was not favorable for the interaction between cerium and manganese oxides and tended to form separate metal oxides.

It was easier for mercury to give an electron than to accept an electron. The strength of the acidic sites on the sorbent surface was important for its mercury adsorption ability accordingly. To investigate the cause of the different adsorption performances on $Ce_{0.5}Mn_{0.5}O_y$ at low and high temperatures, NH_3 was pre-adsorbed at 100 and 300 °C. After removal of physically adsorbed NH_3 by helium purge, temperature-programmed desorption curves were recorded to test its NH_3 adsorption ability. As shown in Figure S1, if NH_3 was pre-adsorbed on the sorbent at 100 °C, at least four desorption peaks emerged at 500−800 °C. Comparatively, if NH_3 was pre-adsorbed at 300 °C, most of the desorption peaks disappeared and the remaining peaks were very weak. It illustrated that NH_3 could easily be adsorbed on the acidic sites at a low

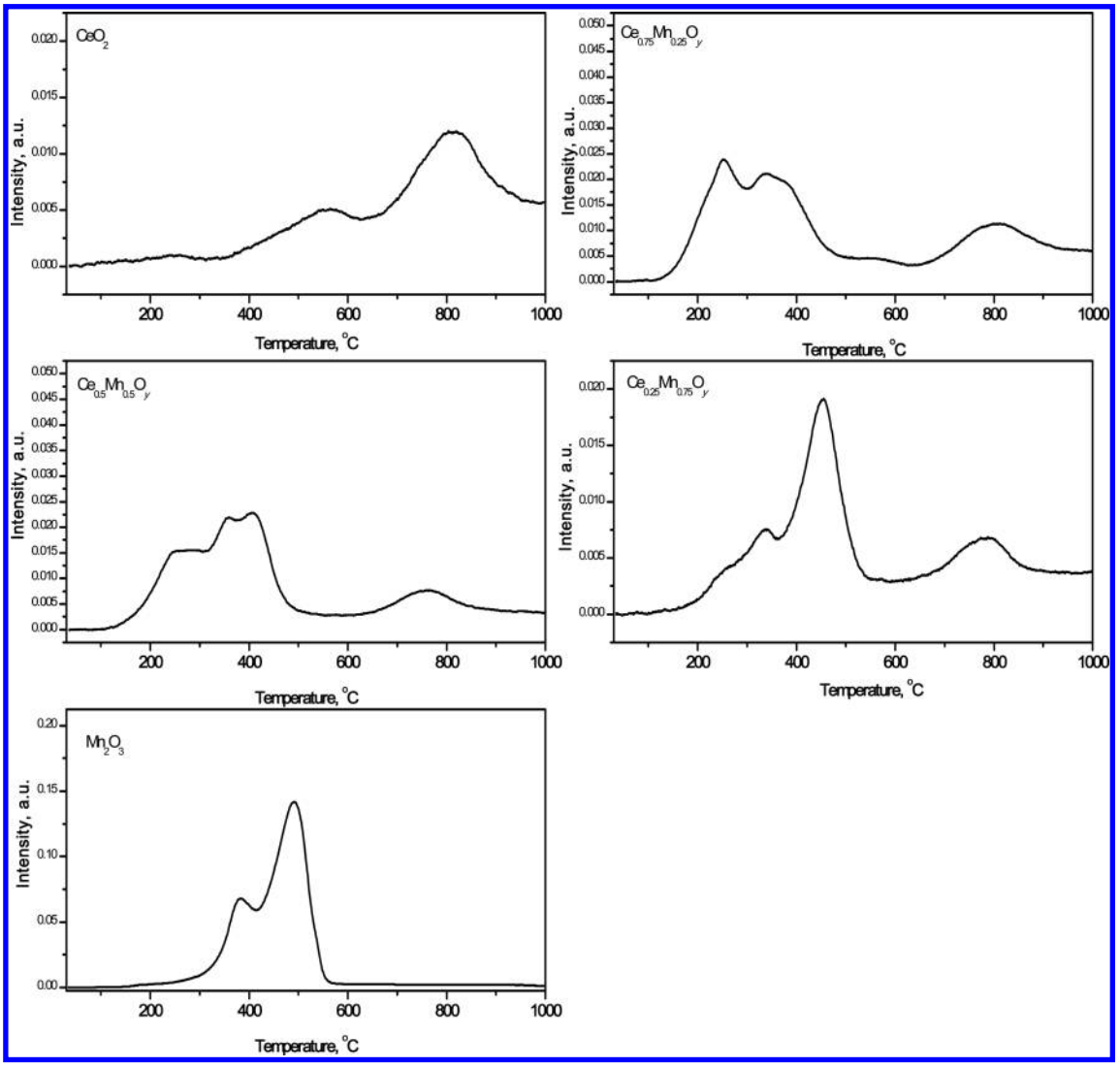

Figure 4. H_2-TPR curve of $Ce_{1-x}Mn_xO_y$ (x = 0, 0.25, 0.5, 0.75, and 1).

DOI: 10.1021/acs.energyfuels.5b00868
Energy Fuels 2015, 29, 6187−6196

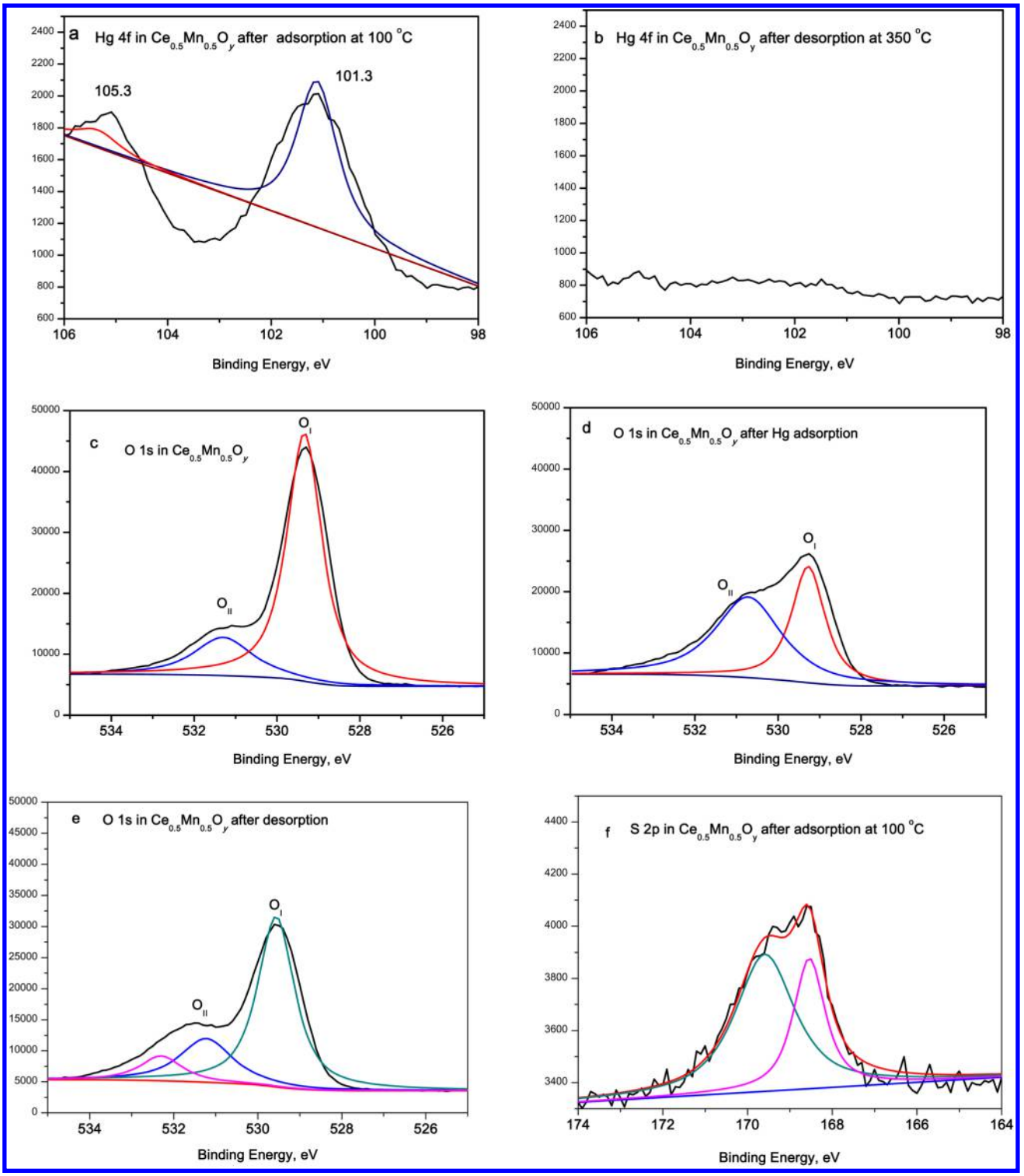

Figure 5. XPS spectra of $Ce_{0.5}Mn_{0.5}O_y$ over Hg 4f, O 1s, and S 2p regions: (a) Hg 4f on $Ce_{0.5}Mn_{0.5}O_y$ after adsorption of mercury at 100 °C, (b) Hg 4f on $Ce_{0.5}Mn_{0.5}O_y$ after desorption at 350 °C, (c) O 1s on fresh $Ce_{0.5}Mn_{0.5}O_y$, (d) O 1s on $Ce_{0.5}Mn_{0.5}O_y$ after mercury adsorption, (e) O 1s on $Ce_{0.5}Mn_{0.5}O_y$ after regeneration, and (f) S 2p on $Ce_{0.5}Mn_{0.5}O_y$ after mercury adsorption.

temperature, whereas most of the acidic sites lose their activity at a high temperature. Furthermore, if the sorbent was pretreated by SO_2 for 3 h, the amount of desorbed NH_3 decreased in comparison to the non-pretreated sample. It is worth noting that some desorption peaks disappeared and the relative strength of peaks at 600 and 700 °C were changed. It was believed that SO_2 could competitively adsorb on partial acidic sites and inhibit the adsorption capability of the sorbent. This result was consistent with the mercury adsorption experiment.

To investigate the pathways for mercury adsorption on the sorbent, XPS was employed to analyze the valence of adsorbed mercury on the sorbent surface, and the results were shown in panels a and b of Figure 5. Two obvious peaks at 101.3 and

DOI: 10.1021/acs.energyfuels.5b00868
Energy Fuels 2015, 29, 6187−6196

Table 2. Surface Ratio of Lattice Oxygen to Defected Oxide Calculated from XPS Results

sample[a]	surface ratio of lattice oxygen to defect oxide (O_I/O_{II}; Figure S6)
fresh $Ce_{0.5}Mn_{0.5}O_y$	3.5
spent $Ce_{0.5}Mn_{0.5}O_y$	0.8
regenerated $Ce_{0.5}Mn_{0.5}O_y$	2.5

[a]Fresh and spent $Ce_{0.5}Mn_{0.5}O_y$ denote the sorbents before and after mercury adsorption, while regenerated $Ce_{0.5}Mn_{0.5}O_y$ denotes the sorbent after mercury desorption.

105.3 eV could be observed on $Ce_{0.5}Mn_{0.5}O_y$ after adsorption of mercury at 100 °C for 10 h in the presence of 500 ppm of SO_2. These two peaks could be attributed to Hg $4f_{7/2}$ and Hg $4f_{5/2}$, respectively. Because no other component can be combined with oxidized mercury, adsorbed mercury was speculated to exist as mercuric oxide (HgO).[28] After desorption at 350 °C, no significant peak corresponding to mercury could be observed in the XPS spectrum of the sorbent over the Hg spectral region. It indicated that almost all adsorbed mercury could release from the sorbent at 350 °C.

Additionally, XPS spectra of O 1s on the sorbent surface were also collected. As shown in panels c–e of Figure 5, the major peak O_I was attributed to lattice oxygen in $Ce_{0.5}Mn_{0.5}O_y$. Peak O_{II} was corresponding to defect oxide or hydroxyl-like groups.[29−31] After adsorption, the lattice oxygen content decreased significantly in comparison to the fresh sorbent (the calculated data were listed in Table 2). It illustrated that lattice oxygen participated in the reaction during the adsorption process. After regeneration at 350 °C, consumed lattice oxygen was complemented. Moreover, after mercury adsorption in the presence of 500 ppm of SO_2, peaks in the S 2p region appeared at 168.7 and 169.9 eV (Figure 5f), which could be attributed to sulfur of SO_4^{2-} and HSO_4^-, respectively.[32] This was consistent with result of the ion chromatogram (Figure S2).

3.2. Hg^0 Adsorption Tests. As shown in Figure 6, pure CeO_2 exhibited negligible adsorption to elemental mercury at a temperature from 100 to 300 °C. In contrast, pure Mn_2O_3 synthesized here had a considerable mercury adsorption capacity at 100 °C (about 3.0 mg g^{-1}), and the doping of cerium could improve the mercury adsorption capability significantly. The adsorption capacity of $Ce_{0.5}Mn_{0.5}O_y$ could reach 5.6 mg g^{-1} at 100 °C, which was the highest among prepared sorbents. Meanwhile, over 98% of mercury removal efficiency could be achieved under 1.0×10^5 h^{-1} space velocity within 10 h. Moreover, the temperature exerted an important impact on the mercury adsorption capacity of the synthesized sorbents. A low temperature facilitated the mercury adsorption on the sorbents. With the increase of the temperature, the adsorption capacity decreased significantly. At 300 °C, only a little amount of mercury could be adsorbed on $Ce_{0.5}Mn_{0.5}O_y$ (the breakthrough curve was also shown in Figure 6). This result was consistent with the NH_3-TPD result that the sorbent lost most of its NH_3 adsorption capability at 300 °C (Figure S1). According to the results above, manganese species in binary metal oxides $Ce_{1-x}Mn_xO_y$ was believed to be the active site for mercury adsorption, and the interaction between manganese and cerium oxides in binary metal oxides could enhance their capacity for mercury adsorption.

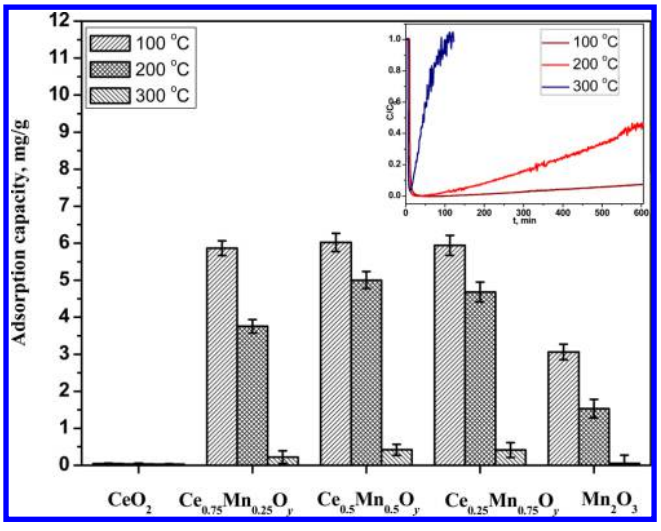

Figure 6. Impact of the temperature on the mercury adsorption capacity of $Ce_{1-x}Mn_xO_y$. Space velocity, 1.0×10^5 h^{-1}; carrier gas, N_2 + 4% O_2; and mercury concentration, 1.05 mg m^{-3}. (Inset) Mercury breakthrough curves on $Ce_{0.5}Mn_{0.5}O_y$ at 100, 200, and 300 °C.

3.3. Impact of Flue Gas Components. The impact of flue gas components on the capacity of sorbents is important for screening material.[33] Thus, the mercury capture peformances of $Ce_{0.5}Mn_{0.5}O_y$ in the presence of O_2, NO, SO_2, and HCl were investigated. As shown in Figure 7, the change of mercury capacity within 10 h was negligible in the presence of 500 ppm of NO. After introduction of 500 ppm of SO_2 into the influent, the mercury capacity on $Ce_{0.5}Mn_{0.5}O_y$ decreased by 1–8% at a temperature from 100 to 150 °C but the capacity was still much higher than reference materials (Table 3). In addition, the effect of O_2 was also investigated. As shown in Figure S4, the experiments were under pure N_2 and N_2 + 4% O_2. The

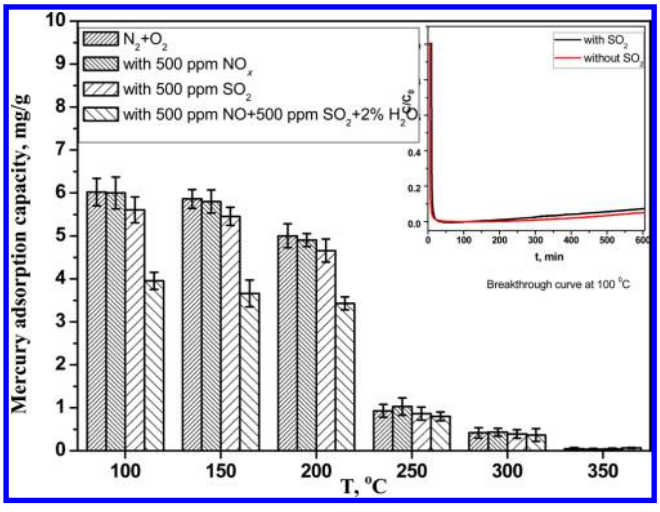

Figure 7. Impact of NO, SO_2, and H_2O on the adsorption capacity of $Ce_{0.5}Mn_{0.5}O_y$ at different test temperatures. Space velocity, 1.0×10^5 h^{-1}; carrier gas, N_2 + 4% O_2; and mercury concentration, 1.05 mg m^{-3}. (Inset) Mercury breakthrough curves on $Ce_{0.5}Mn_{0.5}O_y$ with and without SO_2.

DOI: 10.1021/acs.energyfuels.5b00868
Energy Fuels 2015, 29, 6187–6196

Table 3. Comparison of Mercury Adsorption Capacities between Reference Sorbents and $Ce_{0.5}Mn_{0.5}O_y$

sorbent	capacity (mg g^{-1})	carrier gas	temperature (°C)	regenerability
Cl−AC[26]	4	air	138	no
Z−Ag[034]	0.5	air	150	no
MagZ−Ag[035]	0.044	air	150	yes
$(Fe_{2.2}Mn_{0.8})_{1-\delta}O_4$[32]	1.9	air with SO_2	150	no
$(Fe_2Ti_{0.5}Mn_{0.8})_{1-\delta}O_4$[36]	4.2	air with SO_2	150	no
$Fe_2Ti_{0.6}V_{0.4}O_{4+\delta}$[28]	1	air with SO_2	100	yes
$Ce_{0.5}Mn_{0.5}O_y$ (this paper)	5.6	$N_2 + O_2 + NO + SO_2$	100	yes

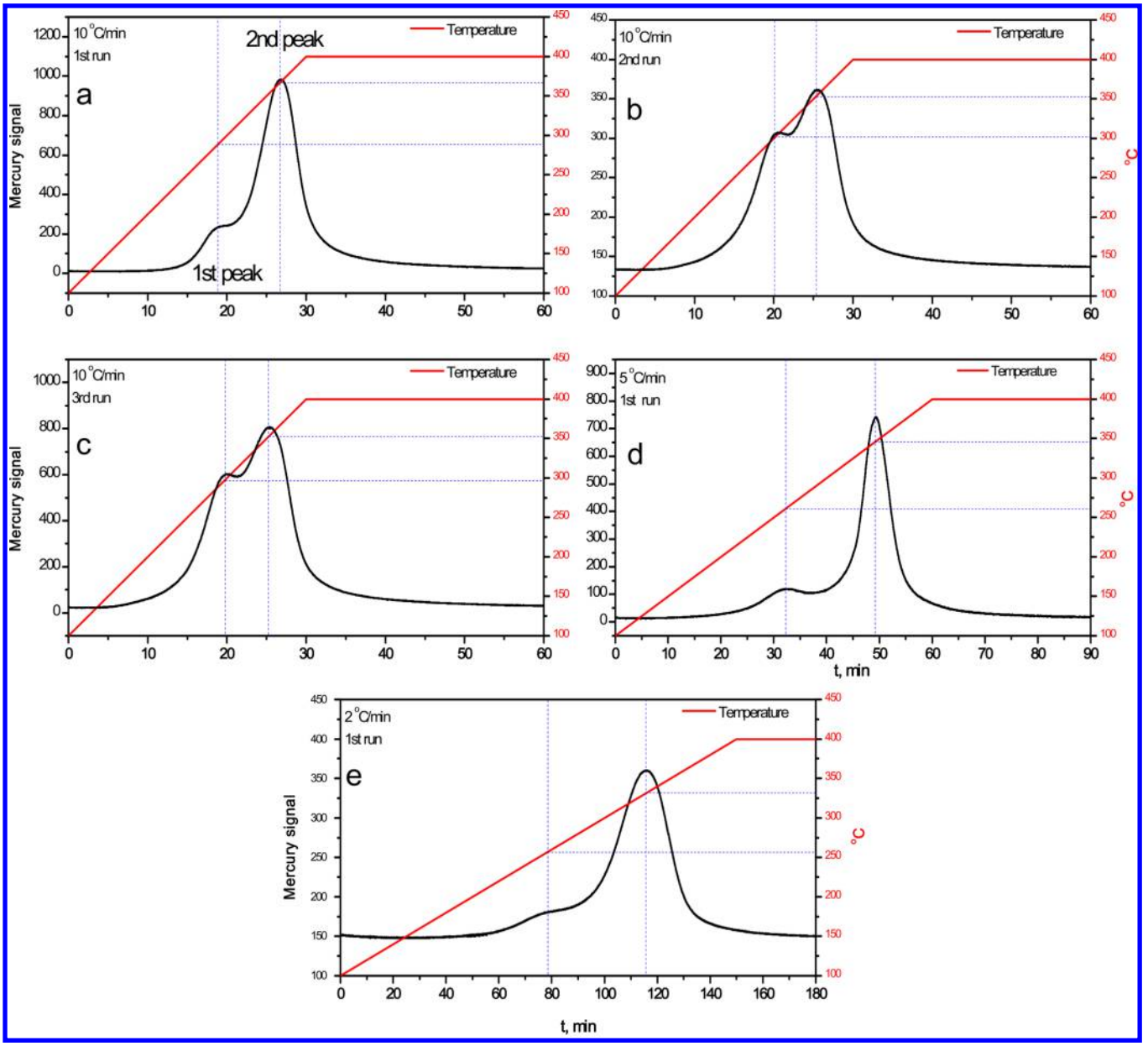

Figure 8. Hg-TPD curves on $Ce_{0.5}Mn_{0.5}O_y$ at different heating rates.

presence of O_2 significantly enhanced Hg^0 removal efficiency. O_2 played an important role during the Hg^0 removal process.[20] The impacts of different concentrations of NO were also tested, and the results are shown in Figure S5. Obviously, NO had negligible impact on mercury adsorption when the concentration of NO was 100 or 500 ppm in the simulated flue gas. This result was also consistent with the NH_3-TPD result that the pre-sulfurized sample showed some decrease on the NH_3 adsorption amount (Figure S1). It was supposed that SO_2 could be adsorbed on part of active sites on the sorbent surface and partially inhibit the access of mercury to the sorbent. The impact of different concentrations of SO_2 (Figure S5) showed that SO_2 was not favorable for Hg^0 capture. The higher the SO_2 concentration, the lower the mercury capacity. Furthermore, the results demonstrated that the mixture of NO, SO_2, and H_2O could enhance this inhibition. It could be the reason for

DOI: 10.1021/acs.energyfuels.5b00868
Energy Fuels 2015, 29, 6187−6196

the fact that H_2O could also be adsorbed on the sorbent surface and decrease the probability for mercury to contact the sorbent surface. The impact of HCl on adsorption capacity of $Ce_{0.5}Mn_{0.5}O_y$ at different test temperatures is shown in Figure S6. Obviously, the mercury capacities dropped with the temperature rising, although HCl promoted the Hg^0 adsorption compared to under N_2 + O_2 conditions.

Disposable sorbents will increase the running cost and bring risk to the environment. If the sorbent can be easily regenerated and used repeatedly, the cost for flue gas mercury capture can be significantly decreased and the process will be more environmental friendly. Because only a little amount of mercury could be adsorbed on $Ce_{0.5}Mn_{0.5}O_y$ at 300 °C, the mercury desorption curve was investigated at a higher temperature (350 °C) to desorb mercury adsorbed on $Ce_{0.5}Mn_{0.5}O_y$ quickly. Figure S3 was the mercury desorption curve from spent $Ce_{0.5}Mn_{0.5}O_y$ at 350 °C under a purge of nitrogen, and adsorbed mercury desorbed quickly in the form of elemental mercury. The concentration of desorbed mercury was very high and overflowed the detecting limit of the detector. It was noted that the desorption of mercury adsorbed on $Ce_{0.5}Mn_{0.5}O_y$ at 200−300 °C was not thorough. When the temperature was elevated to 350 °C, there was still some elemental mercury desorbed. Further elevating the temperature to 400 °C, only little mercury could be detected. Hence, 350 °C was chosen here for sorbent regeneration. Additionally, a high concentration of mercury vapor could be produced by controlling the flow rate of purging nitrogen. It is feasible to recycle this high concentration of elemental mercury by driving the desorbed effluent through a cold trap.

3.4. Mercury Desorption Performance. To further investigate the desorption performance of mercury from the sorbent, a temperature-programmed desorption experiment was carried out. In this experiment, spent $Ce_{0.5}Mn_{0.5}O_y$ sorbent was put into a furnace with a temperature-programmed function (to avoid overflowing the detection limit, the mercury adsorption time was limited to 20 min). Then, Hg-TPD curves under different heating rates were collected, and the results were shown in Figure 8. It could be found that two peaks emerged during the desorption process. This indicated that there were two kinds of adsorption sites on the surface of the sorbent. The higher the temperature at which the desorption peak appeared, the stronger the interaction force between mercury and adsorption sites. Furthermore, it was interesting that, once the sorbent was reused after regeneration, the temperature gap between first and second peaks became narrower. It was speculated that energy rearrangement between mercury and active sites occurred. As a result, the interaction forces of two kinds of adsorption sites toward mercury were homogenized.

Meanwhile, it was found that the heating rate could impact the desorption behavior of mercury from the sorbent surface. The peak position would vary with the change of the heating rate. The faster the heating rate, the higher the temperature at which the desorption peaks appeared. On the basis of the temperature-programmed desorption data, a model was built for evaluation of mercury desorption activation energy from the sorbent surface (see the Supporting Information). The energy could be calculated according to eq 2.[34−36] They were 89.4 and 131.3 kJ mol^{-1} corresponding to first and second desorption peaks, respetively (Table S1).

$$2\ln T_p - \ln \beta = \frac{E_d}{RT_p} + \ln \frac{E_d}{AR} \quad (2)$$

where T_p (K) denotes a certain temperature at which the desorption rate reaches the maximum value, β (K min^{-1}) is the heating rate, E_d is the desorption activation energy (kJ mol^{-1}), R is the gas constant, and A is the pre-exponential factor.

Furthermore, to investigate the reusability of the sorbent, 5 cycles of mecury adsorption and desorption tests were performed through a packed-bed experiment. As shown in Figure 9, the mercury adsorption capacity of fresh $Ce_{0.5}Mn_{0.5}O_y$

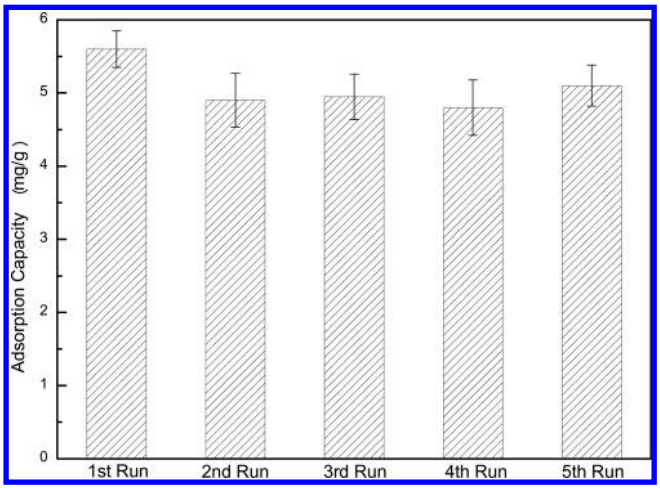

Figure 9. Mercury adsorption capacities on $Ce_{0.5}Mn_{0.5}O_y$ in 5 runs (space velocity, 1.0 × 10^5 h^{-1}; mercury concentration, 1.05 mg m^{-3}; carrier gas, 4% O_2 + 500 ppm of SO_2 + N_2; adsorb mercury at 100 °C and regenerate at 350 °C for each run; and purge gas in the regeneration process, high-purity N_2).

was about 5.6 mg g^{-1}, and the capacity would decrease to about 5.1 mg g^{-1} if used repeatedly. However, the mercury adsorption capacity would not further decline after 5 runs of adsorption. It was possible that SO_2 could only occupy partial active sites for mercury adsorption on the sorbent surface and inhibited the interaction of mercury with the sorbent. Other active sites were still available for mercury. Therefore, the capacity would not decrease further.

3.5. Hg^0 Adsorption Mechanism. On the basis of the experiment and charaterization results, it could be concluded that manganese played a key role on mercury adsorption and oxidation. It was the main active component for mercury adsorption. Meanwhile, cerium could benefit the formation of high surface area material. Moreover, cerium oxides also participated in the regeneration of the sorbents. From the above discussion, the Mars−Maessen mechanism was the possible pathway for elemental mercury capture on Ce−Mn binary metal oxides.[26] The reaction process of mercury with $Ce_{0.5}Mn_{0.5}O_y$ could be described as follows:

$$Hg^0_{(g)} \leftrightarrow Hg^0_{(ad)} \quad (3)$$

$$2Mn^{4+} + \equiv O^{2-} + Hg^0_{(ad)} \leftrightarrow 2Mn^{3+} + HgO_{(ad)} \quad (4)$$

$$2Mn^{3+} + 2CeO_2 \leftrightarrow 2Mn^{4+} + Ce_2O_3 + \equiv O^{2-} \quad (5)$$

$$Ce_2O_3 + \frac{1}{2}O_{2(g)} \leftrightarrow 2CeO_2 \quad (6)$$

DOI: 10.1021/acs.energyfuels.5b00868
Energy Fuels 2015, 29, 6187−6196

First, gaseous elemental mercury was physically adsorbed on the active sites of the sorbent surface through collision (reaction 3). During this physical adsorption process, the higher surface areas of the materials were more favorable for Hg^0 adsorption. The adsorption behavior was an exothermic process; therefore, a higher temperature would be adverse to mercury adsorption. This could explain why the sorbent showed a higher capacity at a low temperature. Second, the adsorbed elemental mercury was oxidized by surface Mn^{4+} with the assistance of lattice oxygen (reaction 4) at a relatively low temperature and trapped on the sorbent surface. Manganese was the primary active site for Hg^0 catalytic oxidation. The higher the valance of Mn, the higher the catalytic oxidation of the catalyst. Reactions 3−6 were all reversible reactions. A low temperature would faciliate reaction 3 to move toward the right side and accumulate a high concentration of adsorbed mercury on the sorbent surface. This high adsorbed mercury concentration on the sorbent surface would further promote reaction 4 toward the right side. When the temperature was elevated, the new reaction balance would be built. Reaction 4 would incline to reverse, and oxidized mercury would be reduced and desorbed as gaseous elemental mercury. Additionally, Mn^{3+} could be oxidized by CeO_2 (reaction 5), and gaseous oxygen would complement consumed lattice oxygen (reaction 6 and Table 2). As shown in XPS analysis, almost all adsorbed mercury could be released from the sorbent surface at 350 °C (Figure 5b). The low valence of Mn (Mn^{3+}) was reoxidized to Mn^{4+}, which indicated that the actice sites can be reactive. Reduced Ce_2O_3 can be reoxidized to CeO_2 by O_2 in the flue gas, resulting in the high capacities of Hg^0 over Ce−Mn binary oxides.

4. CONCLUSION

A series of Ce−Mn binary oxides was synthesized and investigated as regenerable sorbents for elemental mercury adsorption. Specific surface areas of the sorbents could be controlled by adjusting the ratio of cerium in Ce−Mn binary metal oxides. Synthesized binary metal oxides had better mercury adsorption capacity than single metal oxides (CeO_2 and Mn_2O_3) synthesized in the same procedure. $Ce_{0.5}Mn_{0.5}O_y$ displayed the best performance among these sorbents. Its adsorption capacity for elemental mercury reached 5.6 mg g^{-1} at 100 °C. It was also found that a low temperature (100−150 °C) would facilitate mercury adsorption on the sorbent surface. SO_2 could to a certain extent inhibit the adsorption of mercury on the sorbents as a result of its competitive adsorption on active sites. Furthermore, most adsorbed mercury on the sorbents could be reversely released by heating to 350 °C. The regenerated sorbent could be repeatedly used for the next run of mercury adsorption, and the mercury adsorption capacity did not show a significant decrease after 5 runs of adsorption and desorption. Mercury desorption activation energy corresponding to first and second desorption peaks was 89.4 and 131.3 kJ mol^{-1}, respectively.

■ ASSOCIATED CONTENT

Supporting Information

The Supporting Information is available free of charge on the ACS Publications website at DOI: 10.1021/acs.energyfuels.5b00868.

NH_3-TPD curve on $Ce_{0.5}Mn_{0.5}O_y$, ion chromatogram analysis, mercury desorption from $Ce_{0.5}Mn_{0.5}O_y$, impact of gas components over $Ce_{0.5}Mn_{0.5}O_y$, and mercury desorption activation energy calculation (PDF)

■ AUTHOR INFORMATION

Corresponding Author

*Telephone/Fax: +86-21-54745591. E-mail: nqyan@sjtu.edu.cn.

Notes

The authors declare no competing financial interest.

■ ACKNOWLEDGMENTS

This study was supported by the National Basic Research Program of China (973 Program, 2013CB430005), the National Natural Science Foundation of China (51278294), and the High-Tech R&D Program (863) of China (2013AA065403).

■ REFERENCES

(1) Tchounwou, P. B.; Ayensu, W. K.; Ninashvili, N.; Sutton, D. *Environ. Toxicol.* **2003**, *18* (3), 149−175.
(2) Mackey, T. K.; Contreras, J. T.; Liang, B. A. *Sci. Total Environ.* **2014**, *472*, 125−129.
(3) Wang, S.; Zhang, L.; Zhao, B.; Meng, Y.; Hao, J. *Energy Fuels* **2012**, *26* (8), 4635−4642.
(4) Sun, C. G.; Snape, C. E.; Liu, H. *Energy Fuels* **2013**, *27* (7), 3875−3882.
(5) Hu, C. X.; Zhou, J. S.; Luo, Z. Y.; Cen, K. F. *Energy Fuels* **2011**, *25* (1), 154−158.
(6) Xu, W. Q.; Wang, H. R.; Zhu, T. Y.; Kuang, J. Y.; Jing, P. F. *J. Environ. Sci.* **2013**, *25* (2), 393−398.
(7) Chen, W. M.; Ma, Y. P.; Yan, N. Q.; Qu, Z.; Yang, S. J.; Xie, J. K.; Guo, Y. F.; Hu, L. G.; Jia, J. P. *Fuel* **2014**, *133*, 263−269.
(8) Wang, Y. J.; Liu, Y.; Wu, Z. B.; Mo, J. S.; Cheng, B. *J. Hazard. Mater.* **2010**, *183* (1−3), 902−907.
(9) Sun, M. Y.; Cheng, G. H.; Lu, R. J.; Tang, T. M.; Baig, S. A.; Xu, X. F. *Fuel Process. Technol.* **2014**, *118*, 28−33.
(10) Wang, Q. F.; Liu, Y.; Yang, Z. M.; Wang, H. Q.; Weng, X. L.; Wang, Y. J.; Wu, Z. B. *Fuel* **2014**, *134*, 588−594.
(11) Saha, A. *Energy Fuels* **2014**, *28* (6), 4021−4027.
(12) Xie, J. K.; Xu, H. M.; Qu, Z.; Huang, W. J.; Chen, W. M.; Ma, Y. P.; Zhao, S. J.; Liu, P.; Yan, N. Q. *J. Colloid Interface Sci.* **2014**, *428*, 121−127.
(13) Yang, H. Q.; Xu, Z. H.; Fan, M. H.; Bland, A. E.; Judkins, R. R. *J. Hazard. Mater.* **2007**, *146*, 1−11.
(14) Rodríguez-Pérez, J.; Lopez-Anton, M. A.; Díaz-Somoano, M.; García, R.; Martinez-Tarazona, M. R. *Energy Fuels* **2011**, *25* (5), 2022−2027.
(15) Rodríguez-Pérez, J.; López-Antón, M. A.; Díaz-Somoano, M.; García, R.; Martínez-Tarazona, M. R. *J. Hazard. Mater.* **2013**, *260*, 869−877.
(16) Pavlish, J. H.; Sondreal, E. A.; Mann, M. D.; Olson, E. S.; Galbreath, K. C.; Laudal, D. L.; Benson, S. A. *Fuel Process. Technol.* **2003**, *82* (2−3), 89−165.
(17) Thirupathi, B.; Smirniotis, P. G. *Catal. Lett.* **2011**, *141* (10), 1399−1404.
(18) Ji, L.; Sreekanth, P. M.; Smirniotis, P. G.; Thiel, S. W.; Pinto, N. G. *Energy Fuels* **2008**, *22* (4), 2299−2306.
(19) Liu, X. W.; Zhou, K. B.; Wang, L.; Wang, B. Y.; Li, Y. D. *J. Am. Chem. Soc.* **2009**, *131* (9), 3140−3141.
(20) He, C.; Shen, B. X.; Chen, J. H.; Cai, J. *Environ. Sci. Technol.* **2014**, *48* (14), 7891−7898.
(21) Wen, X. Y.; Li, C. T.; Fan, X. P.; Gao, H. L.; Zhang, W.; Chen, L.; Zeng, G. M.; Zhao, Y. P. *Energy Fuels* **2011**, *25* (7), 2939−2944.
(22) Fan, X. P.; Li, C. T.; Zeng, G. M.; Zhang, X.; Tao, S. S.; Lu, P.; Tan, Y.; Luo, D. Q. *Energy Fuels* **2012**, *26* (4), 2082−2089.

DOI: 10.1021/acs.energyfuels.5b00868
Energy Fuels 2015, 29, 6187−6196

(23) Xie, Y. N.; Li, C. T.; Zhao, L. K.; Zhang, J.; Zeng, G. M.; Zhang, X. N.; Zhang, W.; Tao, S. S. *Appl. Surf. Sci.* **2015**, *333*, 59−67.
(24) Li, H. L.; Wu, C. Y.; Li, Y.; Li, L. Q.; Zhao, Y. C.; Zhang, J. Y. *J. Hazard. Mater.* **2012**, *243*, 117−123.
(25) Li, H. L.; Wu, C. Y.; Li, Y.; Zhang, J. Y. *Appl. Catal., B* **2012**, *111*−*112*, 381−388.
(26) Granite, E. J.; Pennline, H. W.; Hargis, R. A. *Ind. Eng. Chem. Res.* **2000**, *39* (4), 1020−1029.
(27) Machida, M.; Uto, M.; Kurogi, D.; Kijima, T. *Chem. Mater.* **2000**, *12* (10), 3158−3164.
(28) Yang, S. J.; Guo, Y. F.; Yan, N. Q.; Wu, D. Q.; He, H. P.; Xie, J. K.; Qu, Z.; Yang, C.; Jia, J. P. *Chem. Commun.* **2010**, *46* (44), 8377−8379.
(29) Chen, H.; Sayari, A.; Adnot, A.; Larachi, F. *Appl. Catal., B* **2001**, *32* (3), 195−204.
(30) Hamoudi, S.; Larachi, F.; Adnot, A.; Sayari, A. *J. Catal.* **1999**, *185* (2), 333−344.
(31) Larachi, F.; Pierre, J.; Adnot, A.; Bernis, A. *Appl. Surf. Sci.* **2002**, *195* (1−4), 236−250.
(32) Yang, S. J.; Yan, N. Q.; Guo, Y. F.; Wu, D. Q.; He, H. P.; Qu, Z.; Li, J. F.; Zhou, Q.; Jia, J. P. *Environ. Sci. Technol.* **2011**, *45* (4), 1540−1546.
(33) Presto, A. A.; Granite, E. J. *Environ. Sci. Technol.* **2007**, *41* (18), 6579−6584.
(34) Liu, Y.; Kelly, D. J.; Yang, H.; Lin, C. C.; Kuznicki, S. M.; Xu, Z. *Environ. Sci. Technol.* **2008**, *42* (16), 6205−6210.
(35) Dong, J.; Xu, Z. H.; Kuznicki, S. M. *Environ. Sci. Technol.* **2009**, *43* (9), 3266−3271.
(36) Yang, S. J.; Guo, Y. F.; Yan, N. Q.; Wu, D. Q.; He, H. P.; Xie, J. K.; Qu, Z.; Jia, J. P. *Appl. Catal., B* **2011**, *101* (3−4), 698−708.

DOI: 10.1021/acs.energyfuels.5b00868
Energy Fuels 2015, 29, 6187−6196